ARTICLE **Open Access**

Flexible calorimetric differential pressure sensor array integrated with a superhydrophobic surface for flight parameter estimation

Xin Ke[1], Yu Gao[1], Zheng Gong[1], Yunfan Li[1], Zihao Dong[1], Bowei Wan[1], Yurun Guo[1] and Yonggang Jiang[1]✉

Abstract

Distributed pressure sensor array is a promising approach for the estimation of flight parameters for small unmanned aerial vehicles. Current flexible pressure sensor arrays are conventionally subjected to limited sensor resolution, poor bending flexibility, and inadequate packaging protection, resulting in insufficient precision for flight parameter estimation. Here we present a high-resolution differential pressure sensor array using a calorimetric measurement method and a multilayer polyimide bonding technique. The proposed differential pressure sensor array reaches a detection limit of 36.5 mPa over a range of 500 Pa and shows high repeatability when attached to varying curved surfaces. In addition, a superhydrophobic packaging is integrated into the sensor fabrication process, endowing it with waterproof capability. Utilizing a multilayer perceptron neural network, we demonstrated the function of the sensor array in estimating airspeeds and angle of attacks, achieving average solving errors of 0.15 m/s and 0.37°, respectively.

Introduction

Estimating flight parameters involving airspeed and angle of attack (AOA) is crucial for flight control. In contrast to conventional high-speed airplanes, small unmanned aerial vehicles (SUAVs) with significantly lower airspeeds are more susceptible to gusty winds and turbulence, making robust flight control a major challenge[1–3]. Inspired by the flow-field sensing mechanism of avians, distributed air data sensing systems were proposed to capture the attitude information of SUAVs[4–7]. Compared with flush air data sensing system that embeds sensors inside the wing[8,9], the new scheme directly attaches the sensor array onto the wing surface, allowing for easier replacement and lower cost. Flexible airflow or pressure sensor arrays can directly detect flow distributions on the wing surface for the estimation of flight parameters. Furthermore, the rich distributed sensor data would present a greater potential for higher fidelity awareness of flight conditions.

The detection principles of typical airflow sensors are primarily thermal[10–13] and biological flow-sensing hairs[14–16], but their sensing elements must be exposed to the external environment, which is prone to irreversible damage. In contrast, the sensing element in a pressure sensor can be embedded in packaging layers for protection. MEMS-based absolute pressure sensor array was reported to detect pressure at various spots on the wing's surface for flight parameter estimation[6,17,18]. Compared to MEMS-based rigid absolute pressure sensors[19,20], flexible absolute pressure sensors are more adaptable to curved surfaces. However, polymer-based absolute pressure sensors were seldom reported, as polymers are prone to air leakage. By linking the pressure measuring chamber through a microchannel, differential pressure (DP) sensors can directly compare the pressure levels of two pressure sites, bypassing the manufacturing challenges of the reference chamber[21–23]. Therefore, flexible DP sensors are promising for application in distributed air data sensing systems.

Among flexible DP sensors, the capacitive transduction mechanism is commonly used for its simple configuration and facile fabrication process. Xiong et al.[24] developed a flexible sensing skin with a capacitive DP sensor array for multifunctional flying perception. Probably due to the
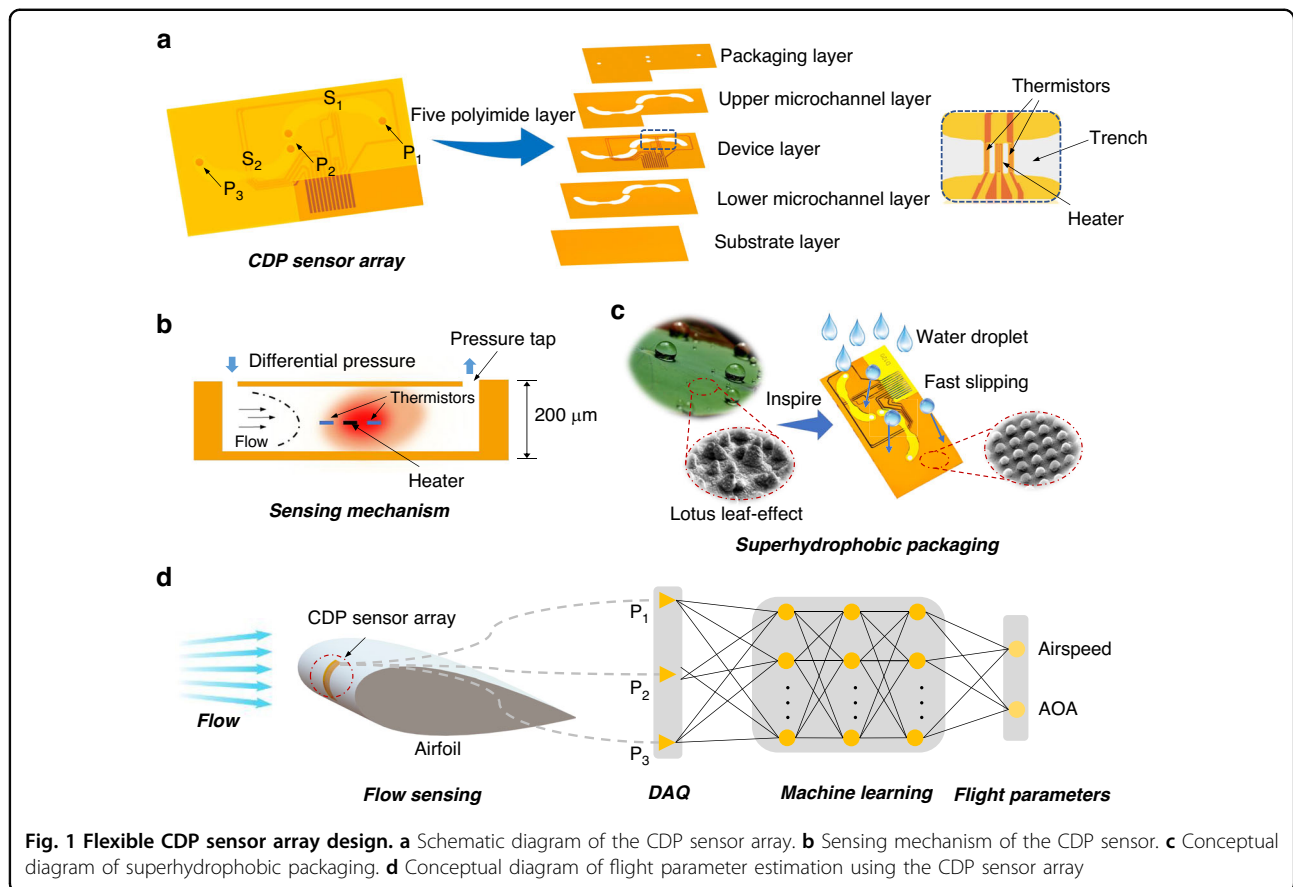
Correspondence: Yonggang Jiang (jiangyg@buaa.edu.cn)
[1]Institute of Bionic and Micro-nano Systems, School of Mechanical Engineering and Automation, 100191 Beijing, China

Fig. 1 Flexible CDP sensor array design. a Schematic diagram of the CDP sensor array. **b** Sensing mechanism of the CDP sensor. **c** Conceptual diagram of superhydrophobic packaging. **d** Conceptual diagram of flight parameter estimation using the CDP sensor array

limited resolution of the flexible DP sensors, the estimation of AOAs and airspeeds was not conducted in their research. Dong et al.[25] presented a sensing fusion methodology for flight parameters using an array of flow and DP sensors. Nevertheless, the low resolution of the DP sensors (~4.5 Pa) hindered the accuracy improvement in solving flight parameters. To improve the resolution of capacitive DP sensors, the aspect ratio of the sensing diaphragm must be increased[21]. However, when coupled to the leading edge of a wing with a considerable curve, the sensing diaphragm with a high aspect ratio deforms due to bending-induced stress. There is still a technological challenge in manufacturing high-sensitivity DP sensing sensors with a flexible package. Recently, a new approach has emerged to achieve DP measurement by sealing thermal flow sensors into pipelines[26]. As the DP sensor uses a hot wire or hot film as the flow-sensing element in a flow channel, it is insensitive to mechanical deformation[27,28]. To the best of our knowledge, flexible calorimetric DP sensing arrays have not yet been reported.

In this paper, we present a flexible calorimetric differential pressure (CDP) sensor array with a high sensitivity and wide detection range. A multilayer polyimide bonding technique was employed to fabricate the sensor array with connected microchannels. Benefiting from the double-

layer microchannels, the sensing element is suspended in the middle of the microchannels, which faces the highest flow velocity inside. The proposed CDP sensor exhibits a high resolution of 36.5 mPa in a detection range of 500 Pa. A multilayer perceptron (MLP) neural network was employed to concurrently calculate the airspeed and angle of attack. In addition, a bioinspired superhydrophobic packaging layer was fabricated, allowing for working normally in raindrop conditions.

Results and discussion
Design of CDP sensor array

The schematic diagram of the proposed CDP sensor array is shown in Fig. 1a. The sensor array consists of three pressure taps (P_1, P_2, P_3) and two identical calorimetric sensing elements (S_1, S_2). It is made up of five polyimide layers, including a substrate layer, a lower microchannel layer, a device layer, an upper microchannel layer, and a packaging layer. The sensing elements are located on the device layer and contain a micro heater in the middle of symmetrically located upstream and downstream thermistors. The heaters and thermistors are isolated from a flexible substrate via trenches to reduce thermal conduction via the polyimide substrate. It is worth noting that the trench matches the geometry of the microchannel, connecting the

upper and lower microchannels. Hence, the sensing elements can be suspended in the middle layer of these dual microchannels. The CDP sensor array converts DP measurements between pressure taps into airflow velocity measurements within the microchannels (Fig. 1b). When the pressure difference between the two ends of the microchannel is zero, the temperature profile with respect to the heater is symmetrically distributed. On the contrary, while there is a pressure difference, the differential thermal temperature (ΔT) of the CDP sensor between upstream and downstream thermistors is related to convective heat transfer. The thermal output ΔT can be further converted to an electrical voltage signal (V_{out}) through a Wheatstone bridge, realizing differential pressure measurement. To enhance the adaptability of the CDP sensor array in complicated surroundings, we proposed a lotus leaf-inspired superhydrophobic packaging that prevents water from entering the microchannels (Fig. 1c). The proposed CDP sensor array can be conformally attached to the leading edge of a SUVA wing, like the receptors on avian wings to detect the flow field (Fig. 1d). The relative airflow and AOA can be estimated using a pre-trained machine-learning-based neural network model.

To improve the sensitivity of CDP sensors, we investigate the relationship between the average airflow velocity and the pressure difference. The formula derivation is described in Note S1 (Supplementary information), and the final formula is written as

$$v = \frac{d^2 \Delta P}{32 \mu l} \tag{1}$$

Here v denotes the average airflow velocity, ΔP denotes the pressure difference between the two ends of the microchannel, μ and l denotes the dynamic viscosity of air and the length of the microchannel, respectively.

d represents the hydraulic diameter as given by Eq. (2).

$$d = \frac{2wh}{w + h} \tag{2}$$

Here, w and h denote the width and height of microchannels, respectively. As w is significantly larger than h, d is simplified to be $2h$, which is unaffected by w. Though the increase of h leads to higher sensitivity, it will also increase the total thickness of the sensor, leading to reduced flexibility of the sensor array. Similarly, though the decrease of l leads to higher sensitivity, it will also decrease the detection range of the sensor. In addition, when the distance between two pressure taps is too close, the pressure difference generated during flight parameter estimation will be very small, affecting the accuracy of airspeed and angle of attack calculations. Taking those factors into consideration, h and l are set to 150 μm and 15 mm, respectively.

To further optimize the microchannel structure and to investigate the ideal spatial position of sensing elements, we performed 3D computational fluid dynamics (CFD), and details can be found in the "Methods" section. A contraction channel configuration ($w_1 = 2$ mm, $w_2 = 1$ mm) was employed to increase the upper limit of flow velocity within microchannels. For comparison, normal straight channel configurations with w of 1 mm and 2 mm, were also designed (Fig. 2a). Figure 2b shows that there is no difference in the airflow velocity when w of normal channel configuration is 2 mm or 1 mm. Compared to normal channel configuration, the ratio of airflow velocity to DP in the contraction channel configuration increased by ~72%. The airflow velocity inside the microchannel decreases from the center towards the wall, as shown in Supplementary Fig. S1. Thus, placing the sensing element in the central area of the microchannel can significantly improve the sensitivity of the sensor. In addition, a thermofluid coupling simulation was per-
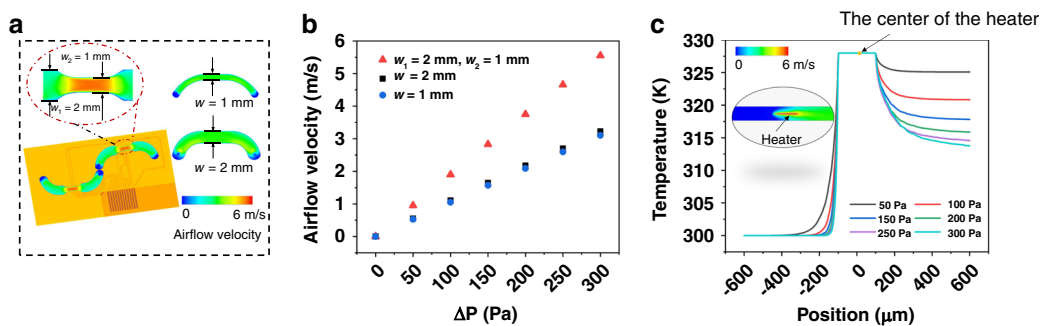

Fig. 2 The CFD simulation analysis. a Simulated cloud map shows the airflow in microchannels with three different configurations. b Simulated airflow velocity curve of three different configurations at the points on the center of the heater. c Simulated airflow velocity curve of three different configurations along the height direction of the microchannel at the center of the heater

formed to evaluate the reasonable distance relationship between the thermistors and the heater. The horizontal axis indicates the horizontal position with the center of the heater as the origin. Figure 2c illustrates that a large ΔT exists when the distance (D) between the heater's edge and the thermistors is less than 200 μm. Based on the above simulation results, the height of the sensing element is designed as $h/2$, and D is designed as 180 μm. Considering the wing section for wind tunnel experiments, the length of the microchannel is designed to be 12 mm, and the overall size of the CDP sensor array is designed to be 30 mm × 16.5 mm × 0.2 mm, with the five polyimide layers from the bottom to the top of 10 μm, 70 μm, 10 μm, 70 μm, and 30 μm, respectively.

Fabricating of CDP sensor array

The fabrication process of the CDP sensor array is schematically illustrated in Supplementary Fig. S2, and details can be found in the "Methods" section. We utilized a conventional MEMS technology to fabricate the device layer and the packaging layer of the CDP sensor array. Starting from the fabrication of the device layer, a polyimide layer with a thickness of 10 μm is spin-coated onto a single-crystalline silicon wafer (Fig. S2A$_1$). Next, Pt-based sensing elements and electrode leads are formed by photolithography, sputtering, and lift-off processes (Fig. S2A$_2$). A thin polyimide layer for insulation and protection is then formed by spin-coating (Fig. S2A$_3$). In the subsequent step, a layer of photoresist is patterned by photolithography and plasma etching is conducted to form the trench structures and expose the electrode pads (Fig. S2A$_4$)). Figure 3a shows the sensing element and trench profile on the device layer, and Fig. 3b shows the serpentine temperature compensation resistor. Finally, the device layer of the CDP sensor array is peeled from the wafer. To simplify the process steps, the upper and lower microchannel layers, as well as the substrate layer, are made of PI film via UV laser ablation.

For the packaging layer, we started to create the negative template of the lotus leaf-like microemulsion array obtained by photolithography and etching on a silicon substrate (Fig. S2B$_{1-3}$). Then, the polyimide is spin-coated and cured on the negative template as the packaging layer and the etching process is used to fabricate the pressure taps (Fig. S2B$_4$). This process is followed by multilayer polyimide bonding, in which five polyimide layers are integrated in a sequential order. A thermo-compression bonding machine was utilized to apply heat and pressure to tightly bond the PI layers. To begin, after coated with fluorinated ethylene propylene (FEP) adhesive uniformly, the overlapped PI layer composed of the substrate layer, lower microchannel layer, and device layer was heated with certain pressure and cooled down naturally with pressure unchanged (Fig. S2C). After the first thermal

bonding, three PI layers were bonded firmly with each other as a flow sensor array, with the sensing element suspended above the lower microchannel layer (Fig. 3c). Next, a second thermal bonding was performed as described above method to package the flow sensor array and turn it into a CDP sensor array (Fig. S2D). During this step, the flow sensor array and upper microchannel layer are sequentially stacked on the packaging layer that remains on the negative template. As a result, the surface of the packaging layer suffers consistent strain, and the micro-cone structure does not distort under high pressure. Figure 3d demonstrates the CDP sensor array stripped from the negative template, which is sufficiently flexible to be attached to curved surfaces. The surface of the packaging layer is covered with closely arranged bionic micro-cone arrays, and the optical image of the pressure tap is shown in Fig. 3e.

Given the vast amount of nanoscale villi growing on microscale papillae arrays on the surface of the lotus leaf, the superhydrophobic feature is attained through the collaboration of micro-nanostructures[29]. Inspired by this, we imitated the micro-nano coordination structure by spin-coating the silicon dioxide dispersion on the CDP sensor array to further enhance the hydrophobic performance of the packaging layer. Scanning electron microscope (SEM) images indicate that the micro-cone array is arranged in order with nanoparticles uniformly wrapped around the surface of the micro-cones (Fig. 3f). The diameter of each micro-cone is 10 μm, the height is 8 μm, and the distance between neighboring micro-cones is 10 μm. In addition, the hydrophobicity of the packaging layer with the bionic surface is characterized, with a smooth surface and micro-coned surface for comparison. The smooth surface refers to polyimide films without micro-nanostructures, and the micro-coned surface refers to the as-prepared packaging layer without coating silica nanoparticles. The left and right static contact angles of water droplets on the bionic packaging layer are 150.5° and 150.7°, respectively (Fig. 3g$_3$), while the values are 80.8° and 80.9° for smooth, 106.7° and 106.5° for micro-coned surface (Fig. 3g$_2$). The superhydrophobic characteristic of the packaging layer with bionic surface is due to the combination effect of the micro-cone array and silica nanoparticles.

Characteristics of CDP sensor

Wind tunnel testing was conducted to assess the performance of the CDP sensor. A feedback circuit was used to enable the CDP sensor to operate in the constant-temperature-difference mode, while the pair of thermistors were connected to differential amplifier circuits (Supplementary Fig. S3). The voltage variation (ΔV) of the CDP sensor exhibits a significant monotonic trend within the DP range of 0–500 Pa, as shown in Fig. 4a. Figure 4b
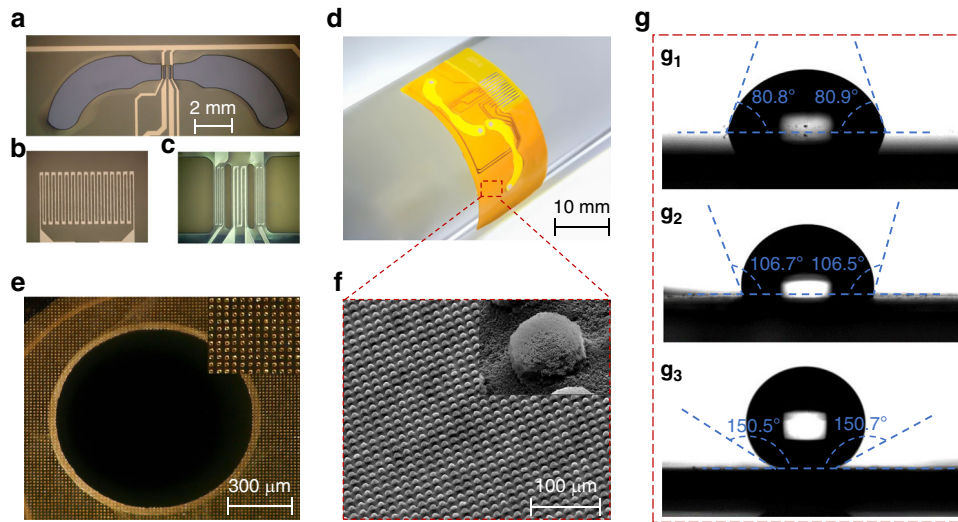
Fig. 3 Photos and contact angle characterization of CDP sensor array. a Optical images of the sensing elements and trench profiles on the device layers. **b** Optical image of the serpentine temperature compensation resistor. **c** Optical image of the sensing element on the CDP sensor array precursor. **d** CDP sensor array attached to a glass cylinder with a radius of 20 mm. **e** Optical images of the pressure tap on the sensor array precursor. **f** SEM images of the micro-cone array on the CDP sensor array after spin-coating silicon dioxide dispersion. **g** Photographs of water droplet contact angles on three surfaces (smooth surface, micro-cones surface, and bionic surface)
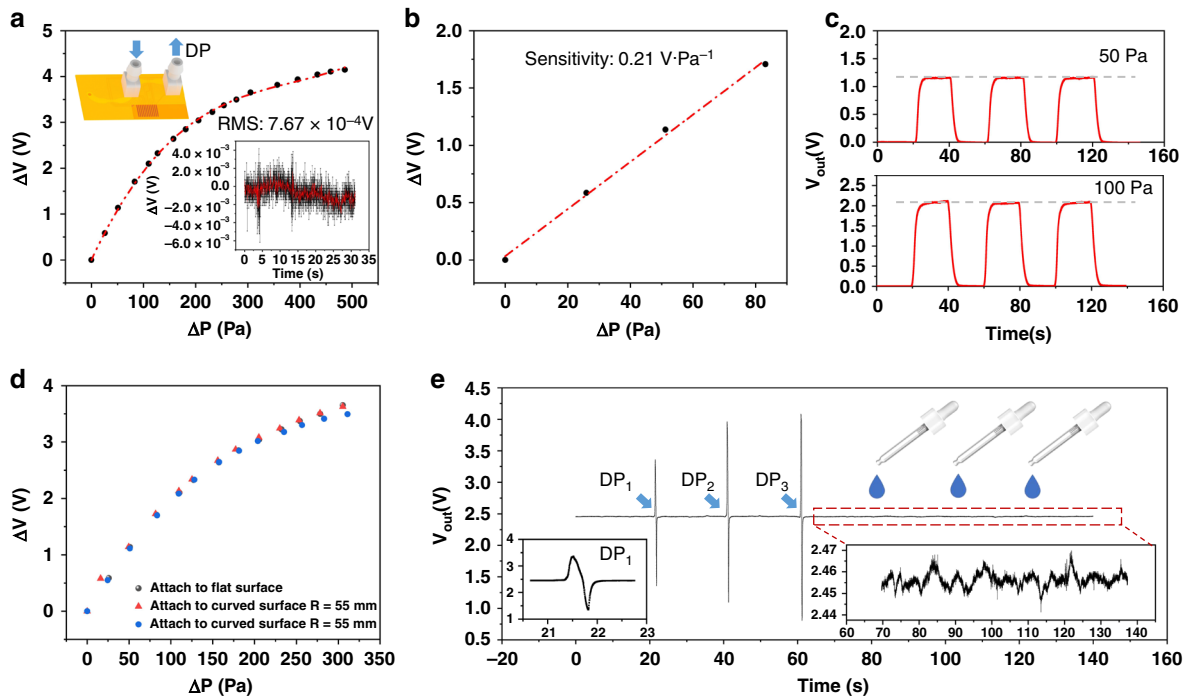

Fig. 4 Characterization and performance of CDP sensor array. a ΔV of the DP sensor varies with DP. **b** Output voltages of CDP sensor is linear in the range of 0–80 Pa. **c** Output voltages of CDP for cyclic loading at different DP of 50 Pa and 100 Pa. **d** ΔV varies with the DP when the CDP sensor is attached to three types of surfaces (flat surface, curved surface $R = 55$ mm, and curved surface $R = 35$ mm). **e** Output voltages of the CDP sensor array under three DP incentives and three water drop incentives

shows that the output of the CDP sensor is linear in the range of 0–80 Pa with a sensitivity of 0.021 V·Pa⁻¹. The minimum detectable DP is calculated to be 36.5 mPa based on the noise level of the sensor (0.767 mV). The CDP sensor exhibits a highly repeatable response when subjected to cyclic differential pressure of 50 and 100 Pa

as shown in Fig. 4c. The standard deviations were ~0.63% of the measured DP values. In addition to the merits of high sensitivity and repeatability, bending adaptability is another important parameter for the proposed CDP sensors, as the CDP sensor array needs to be attached to the leading edge of the wing model. We attached the CDP sensor to cylinders with radii of 35 mm and 55 mm for differential pressure testing. Figure 4d demonstrates that the ΔV of the CDP sensor remained constant under varying degrees of bending, showing the high bending adaptability of the CDP sensor array.

To verify the protection capability of the packaging layer with bionic surfaces, we recorded the response of the sensor as water droplets continuously slid down the pressure tap (Supplementary Movie 1). To demonstrate that the sensor operates normally, we initially applied DP stimulations three times using a small airbag, each separated by ~20 s. Under three DP (DP_1, DP_2, DP_3) stimulations, the sensor exhibits a notable response as shown in Fig. 4e. The enlarged inset of DP_1 shows that the signal first rises, then falls, and finally stabilizes. This is because under the pressure difference stimulation of the small airbag, positive pressure first forms locally in the pressure tap, and negative pressure forms locally in the pressure tap when the airbag deformation recovers. Then we used a dropper to drip water at the pressure measuring hole three times, each separated by ~20 s. The sensor output is almost unaffected, due to the water droplet immediately falls off the surface of the CDP sensor array and is prevented from entering the microchannel. Without superhydrophobic protection, rainwater may get into the microfluidic channel and disrupt the interaction between the temperature and flow fields, causing the sensor to malfunction. The superhydrophobic packaging protects the sensor array from rainwater interference for practical applications.

Supplementary Table S1 presents comprehensive comparisons of the flexibility, sensing modalities, minimum resolution, and detection ranges of reported DP sensors. Our CDP sensor shows the advantage of high sensitivity, benefiting from the suspended sensing elements and contraction channel configuration.

Estimation of flight parameters

The CDP sensor array was attached to the leading edge of a 3D-printed NACA 0016-MOD wing model to estimate flight parameters (Fig. 5a). The S_1 was located on the upper side of the leading edge of the wing, while S_2 was located on the lower side of the leading edge of the wing. For S_1, we designed the P_1 as the high-pressure end and P_2 as the low-pressure end. That is, when the pressure at P_1 is higher, the ΔV is positive, and vice versa. For S_2, P_2 is designed as the high-pressure end and P_3 is set as the low-pressure end (Fig. 1a). The experimental conditions were

set to an airspeed range of 6.5 m/s to 30 m/s and an angle of attack variation from -16° to 16°. Figure 5b, c depicts the real-time variation of V_{out} of S_1 and S_2 with varying AOA under different airspeeds. It can be seen that the output signal is very stable, and the entire process exhibits a distinct step-change trend. For the convenience of neural network calculations, the average of V_{out} under various conditions was calculated, and ΔV was employed to represent changes in S_1 and S_2 with AOA at different wind speeds, as shown in Fig. 5d, e. The initial state of AOA is $-16°$, with P_1 having the highest pressure, followed by P_2, and P_3. As a result, the initial values of both S_1 and S_2 are positive. As AOA gradually increases from $-16°$ to 16°, the stagnation point at the leading edge gradually approaches P_3. As a result, throughout the process, the local pressure of P_3 increases, P_2 first increases and then declines, and P_1 continues decreasing. In the case that AOA is $-8°$, the ΔV of S_1 transitions from positive to negative, indicating that the pressure of P_2 begins to exceed that of P_1. When AOA reaches 14°, the ΔV of S_2 transitions from positive to negative, indicating that the pressure of P_3 begins to exceed that of P_2. In the variation of AOA from -16 to 16°, ΔV of both S_1 and S_2 decreases monotonically. The stable output variation with wind speeds and AOAs provides effective support for subsequent neural network predictions of AOA and airspeed. Notably, due to the high sensor resolution, there is a noticeable step response during the change of AOA from -16 to 16° at a low wind speed of 6.5 m/s. In previous literature, the lowest airspeed for flight parameter estimation is 10 m/s. It suggests that the novel CDP sensor array is applicable for low airspeed applications.

An MLP neural network was employed to train test data and predict flight parameters owing to its adaptive learning abilities, robustness to noise, and simple structure. The pressure data serve as the input layer, and the MLP neural network outputs are airspeed and AOA. As shown in Fig. 5f, the training set consists of 90 sets of data collected from airspeeds ranging from 6.5 to 30 m/s with AOA of 0, ± 6°, ± 10°, ± 14°, and ±16°. The testing set includes 80 sets of data collected at AOA of ±2°, ±4°, ±8°, and ±12°, with airspeeds ranging from 6.5 to 30 m/s.

The calculated errors were obtained by comparing the results with the actual values of the test set to determine the estimation accuracy. The estimated values of the AOA and airspeed for all the test points agree well with the actual, as shown in Fig. 5g. The maximum error value of airspeed is less than 0.57 m/s, and the average error value is 0.15 m/s (Fig. 5h). The maximum error value of AOA is less than 1.46°, and the average error value is 0.37° (Fig. 5i). Supplementary Table S2 lists the relevant studies on the sensing array used for SUAV, and this study demonstrates leading prediction accuracy and wide airspeed range.
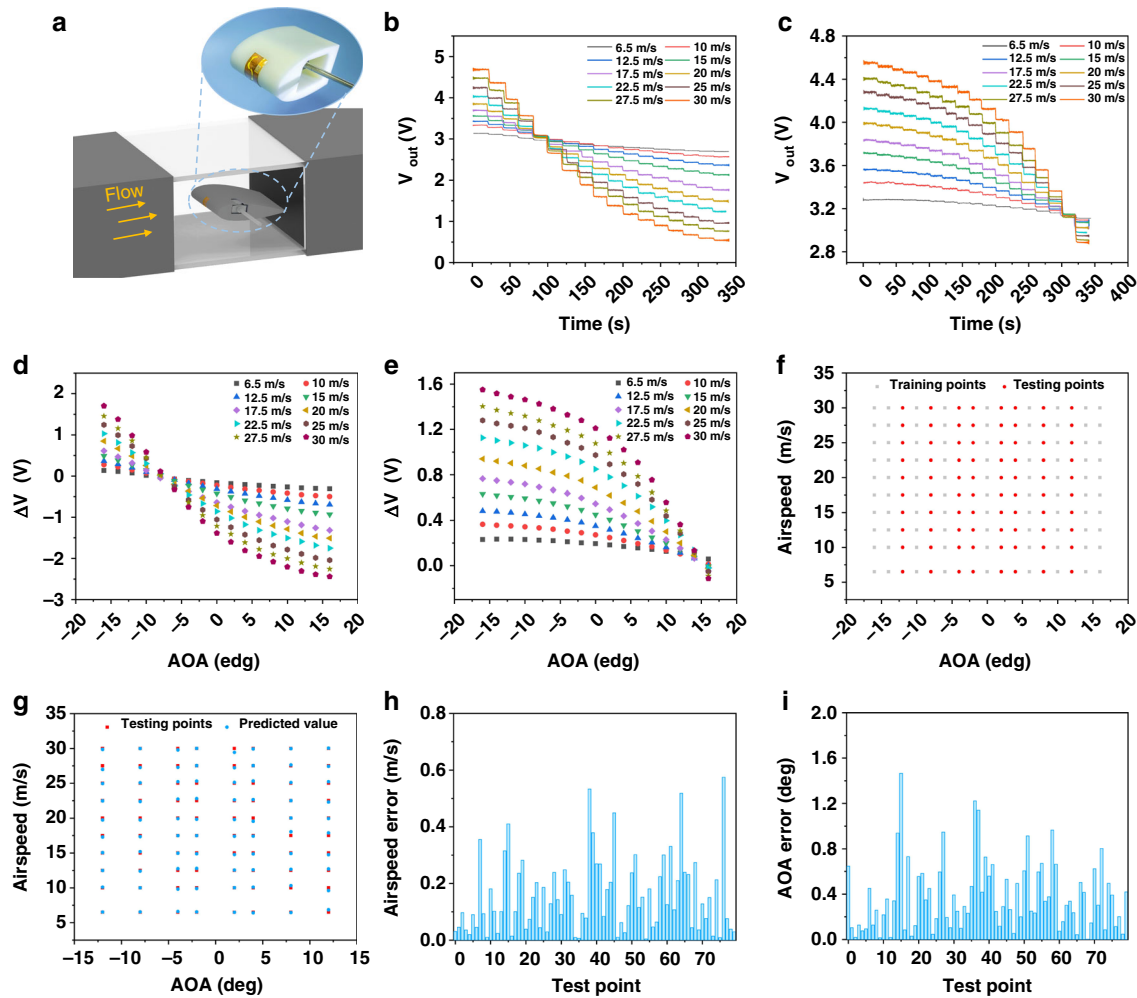
Fig. 5 Estimation of airspeed and AOA using a CDP sensor array. a Schematic of the experimental setup for airspeed and AOA predictions, where the CDP sensor array was attached to a NACA 0024-MOD airfoil. **b** Real-time variation of S_1 varies with different airspeed and AOA. **c** Real-time variation of S_2 varies with different airspeed and AOA. **d** ΔV of S_1 varies with different airspeed and AOA. **e** ΔV of S_2 varies with different airspeed and AOA. **f** Training (gray) and testing (red) points for different airspeed and AOA from −16 to +16°. **g** Testing (red)and predicted (blue) points for different airspeed and AOA from −16 to +16°. **h** Absolute airspeed error results. **i** Absolute AOA error results

Conclusion and outlook

In summary, a flexible CDP sensor array integrated with a superhydrophobic surface was developed for flight parameter estimation. The proposed CDP sensor achieved a high resolution (36.5 mPa), and a wide range (0–500 Pa). The CDP sensor array was mounted onto the leading edge of a wing model to measure the pressure distribution and estimate the flight parameters via an MLP neural network. It is worth mentioning that the output response of the sensing skin in a bent state is consistent with that in a straight state. The experimental results demonstrated that the average solution errors for the airspeed and AOA in the range of 6.5–30 m/s are as small as 0.15 m/s and 0.37°, respectively.

This excellent sensing performance is attributable to the sensing element being positioned in the area of maximum

flow velocity within the microchannel, as seen clearly in the simulation results. The heater and thermistors are wrapped in two layers of polyimide protection, with a trench divided between them for thermal insulation. The entire sensing element is positioned in the middle of the height direction of the microchannel, making it challenging to produce such a complicated spatial structure using typical surface microfabrication technology. Therefore, we creatively proposed a multilayer polyimide bonding technique to develop to solve this problem. Our proposed suspended configuration within the microchannel reduces thermal conduction from the polyimide substrate and enhances convective heat transfer via both the upstream thermistor and downstream thermistor. Furthermore, a microchannel with a contraction channel configuration was adopted to significantly increase the airflow velocity

in the sensing element area, with a 72% increase in the flow velocity to DP ratio. In addition to high-sensitivity characteristics, a bioinspired micro-nanostructure was developed on the surface of the packaging layer to make it superhydrophobic, with a contact angle of 150.7°. To sum up, our research on highly sensitive CDP sensor arrays with superhydrophobic packaging suggests promising strategies for flight sensing methods in SUAVs, allowing mobility and flexibility in the outdoor complicated environment. It should be noted that the temperature and humidity may vary with time in the actual flight environment. In addition to effective packaging protection, flexible sensor arrays should be calibrated with temperature and humidity, and temperature-humidity multimodal sensors should be integrated into the system to improve the accuracy in flight parameter estimation.

Methods

CFD simulation analysis

To analyze the link between airflow velocity in microchannels and pressure difference at both ends of the pressure taps, we performed a 3D fluid CFD simulation. For simulations of contraction channel configurations ($w_1 = 2$ mm, $w_2 = 1$ mm) and normal straight channel configurations with w of 1 mm and 2 mm, the computational domains were consistent with the corresponding configurations, and applied boundary conditions were kept consistent. The dynamic viscosity and density of air are set to 1.79×10^{-5} and 1.29 kg/m^3, respectively. As the Reynolds number is below 100, the laminar flow model is selected for calculation. The inlet was defined on the left pressure tap of the computational domain to apply the incoming pressure. The curve was obtained by extracting the airflow velocity at the center of microchannels with three designed structures under pressure difference from 0 to 300 Pa. To investigate the reasonable distance relationship between the thermistors and heater, a 3D thermofluid coupling CFD simulation was performed. The computational domain was consistent with a reduced diameter configuration ($w_1 = 2$ mm, $w_2 = 1$ mm), and the heater was applied to a temperature of 328 K.

Fabrication process

The polyimide precursor solution was spin-coated at 3000 rpm for 30 s on the silicon wafer and then cured at temperatures of 70, 140, 210, and 280 °C, for 30 min to form the supporting of the device layer. A lift-off process was employed to form electrodes and resistive heater metal layers (Ti/Pt; 20 nm/300 nm), and thermistor metal layers (Ti/Pt; 20 nm/50 nm)) were also patterned using a lift-off process. Then, a second layer of polyimide was spin-coated and cured to form the protective of the device layer. Both the supporting and protective polyimide layers were patterned using reactive ion etching in O$_2$/SF$_6$ gas at ambient temperature for 40 min. After 5 min of alcohol ultrasonic cleaning, the polyimide layer was peeled from the silicon wafer to form the device layer. The negative template was obtained by silicon wafers that were patterned using reactive ion etching in O$_2$/SF$_6$ gas at ambient temperature for 10 min. Then, a layer of release agent was sprayed on the negative template (FKL-1846). The polyimide precursor solution was spin-coated at 1500 rpm for 30 s on the template and then cured according to the above process. Then, the pressure taps and packaging layer contours were patterned by photolithography and subjected to reactive ion etching in O$_2$/SF$_6$ gas for 80 min. For the thermal bonding process, with temperature and pressure set to 200 °C and 2 MPa, respectively. The silicon dioxide dispersion employing a solution volume ratio of perfluorosilane: silicon dioxide nanoparticles (20 nm diameter):ethanol = 1:10:100, mixed for 6 h with a magnetic stirrer, then sonicated for 1 hour. Finally, we spin-coated the silicon dioxide dispersion over the device surface at 500 rpm before drying it at 100 °C for 5 min to obtain a full CDP sensor array.

Characterization of the CDP sensor

The performance of the CDP sensor was characterized using a desktop wind tunnel (WT4401-D, OMEGA, USA) that can provide constant pressure. In the calibration of the pressure sensors, the wind tunnel's low-pressure end was supplied into a pressure tap connected to the sensor via a conduit as a reference pressure, while the other pressure tap was supplied to the high-pressure end. The 3D-printed ventilation chambers were attached to the CDP sensor array utilizing epoxy resin, and the ventilation chambers can be connected to the pressure end of the wind tunnel through flexible tubes to introduce pressure. The pressure difference was adjusted by changing the wind tunnel velocity and quantified by employing a commercial DP sensor. The CDP sensor array is connected via a flexible flat cable to the circuit board, which integrates a constant-temperature difference heating circuit and a temperature measurement circuit. The output signal of the CDP sensor was input into a DAQ card (USB-6366, NI) through a differential amplifier circuit, acquired by the host computer, and then subjected to 5 Hz low-pass digital filtering.

Characterization of the CDP sensor array

The CDP sensor array was attached to the leading edge of a 3D-printed NACA 0016-MOD wing as a test prototype, which was then inserted into the wind tunnel and attached to a rotating micro-positioner. This manipulation allows precise control of the AOA, varying between −16° and 16°. The output signal of the CDP sensor array was input into a DAQ card (USB-6366, NI) through a differential amplifier circuit, acquired by the host computer, and then subjected to 5 Hz low-pass digital filtering.

References
1. Lian, Y., Shyy, W., Viieru, D. & Zhang, B. Membrane wing aerodynamics for micro air vehicles. *Prog. Aerosp. Sci.* **39**, 425–465 (2003).
2. Fei, H., Zhu, R., Zhou, Z. & Wang, J. Aircraft flight parameter detection based on a neural network using multiple hot-film flow speed sensors. *Smart Mater. Struct.* **16**, 1239–1245 (2007).
3. Haneda, K. et al. Compact sphere-shaped airflow vector sensor based on MEMS differential pressure sensors. *Sensors* **22**, 1087 (2022).
4. Callegari, S. et al. Aircraft angle of attack and air speed detection by redundant strip pressure sensors. *Proc. IEEE Sens.* **1-3**, 1526–1529 (2004).
5. Zagnoni, M. et al. A non-invasive capacitive sensor strip for aerodynamic pressure measurement. *Sens. Actuators A: Phys.* **123–124**, 240–248 (2005).
6. Na, X. et al. Flexible skin for flight parameter estimation based on pressure and velocity data fusion. *Adv. Intell. Syst.* **4**, 2100276 (2022).
7. Dong, Z., Shen, D., Gong, Z., Zhang, D. & Jiang, Y. A flexible flow sensor for detecting airflow velocity and incident angle. *IEEE Sens. J.* **22**, 15884–15892 (2022).
8. Benedetti, D. M. & Veras, C. A. G. Wind-tunnel measurement of differential pressure on the surface of a dynamically inflatable wing cell. *Aerospace* **8**, 34 (2021).
9. Gavrilovic, N., Bronz, M., Moschetta, J.-M. & Benard, E. Bioinspired wind field estimation—part 1: angle of attack measurements through surface pressure distribution. *Int. J. Micro Air Veh.* **10**, 273–284 (2018).
10. Pang, P. et al. Flexible skin for measurement of boundary layer state and flight attitude identification on UAV. *Smart Mater. Struct.* **32**, 045008 (2023).
11. Gong, Z. et al. Flexible calorimetric flow sensor with unprecedented sensitivity and directional resolution for multiple flight parameter detection. *Nat. Commun.* **15**, 3091 (2024).
12. Zhu, R., Que, R. & Liu, P. Flexible micro flow sensor for micro aerial vehicles. *Front. Mech. Eng.* **12**, 539–545 (2017).
13. Sun, B. et al. High sensitive flexible hot-film sensor for measurement of unsteady boundary layer flow. *Smart Mater. Struct.* **29**, 035023 (2020).
14. Shen, D. et al. Bio-inspired flexible airflow sensor with self-bended 3D hair-like configurations. *J. Bionic Eng.* **19**, 73–82 (2022).
15. Sundin, J., Kokmanian, K., Fu, M. K., Bagheri, S. & Hultmark, M. A soft material flow sensor for micro air vehicles. *Soft Robot.* **8**, 119–127 (2021).
16. Dijkshoorn, A., Cui, J., Stramigioli, S. & Krijnen, G. First results of a Soft, 3D-printed, resistive cantilever flow sensor. In *2021 IEEE International Conference on Flexible and Printable Sensors and Systems* 1–4 (IEEE, 2021).
17. He, S., Yunjun, X. & Remeikas, C. Hardware design and validation of pitching control for micro air vehicles using only pressure information. In *IEEE 2013 American Control Conference* 5568–5573 (2013).
18. Wood, K. T., Araujo-Estrada, S., Richardson, T. & Windsor, S. Distributed pressure sensing–based flight control for small fixed-wing unmanned aerial systems. *J. Aircr.* **56**, 1951–1960 (2019).
19. Han, X. et al. Design and experiment of a touch mode MEMS capacitance vacuum gauge with square diaphragm. *Sens. Actuators A: Phys.* **313**, 112154 (2020).
20. Xu, M. et al. Design and fabrication of a MEMS capacitance vacuum sensor based on silicon buffer block. *J. Microelectromech. Syst.* **29**, 1556–1562 (2020).
21. Ke, X. et al. Design and fabrication of a differential pressure MEMS capacitance diaphragm gauge based on heavily boron-doping technique. *Vacuum* **184**, 109880 (2021).
22. Zhao, P., Wu, P., Zhang, D., Ding, X. & Jiang, Y. Cantilever-based differential pressure sensor with a bio-inspired bristled configuration. *Bioinspir. Biomim.* **16**, 055011 (2021).
23. Ke, X. et al. Highly sensitive differential pressure sensor with bristled cantilever configuration using a silicon piezoresistor on polyimide technique. *IEEE Sens. J.* **23**, 22263–22269 (2023).
24. Xiong, W. Bio-inspired, intelligent flexible sensing skin for multifunctional flying perception. *Nano Energy* **90**, 106550 (2021).
25. Dong, Z. et al. Ultrathin flexible skin with all-polyimide pressure and airflow sensor array for estimation of flight parameters. *IEEE Sens. J.* **23**, 29494–29501 (2023).
26. Watanabe, K., Kurihara, Y., Kobayashi, K. & Suzuki, K. In-bed biosignal acquisition from conventional differential pressure sensor based on thermal flow principle. *IEEE Sens. J.* **21**, 5340–5348 (2021).
27. Piotto, M., Del Cesta, S. & Bruschi, P. A compact, dual channel flow-based differential pressure sensor with mPa resolution and sub-10 mW power consumption. *Procedia Eng.* **168**, 757–761 (2016).
28. Xu, W. et al. Systematic study of packaging designs on the performance of CMOS thermoresistive micro calorimetric flow sensors. *J. Micromech. Microeng.* **27**, 085001 (2017).
29. Darmanin, T. & Guittard, F. Superhydrophobic and superoleophobic properties in nature. *Mater. Today* **18**, 273–285 (2015).